

# Journal of Materials Chemistry A

Accepted Manuscript



This is an *Accepted Manuscript*, which has been through the Royal Society of Chemistry peer review process and has been accepted for publication.

*Accepted Manuscripts* are published online shortly after acceptance, before technical editing, formatting and proof reading. Using this free service, authors can make their results available to the community, in citable form, before we publish the edited article. We will replace this *Accepted Manuscript* with the edited and formatted *Advance Article* as soon as it is available.

You can find more information about *Accepted Manuscripts* in the [Information for Authors](#).

Please note that technical editing may introduce minor changes to the text and/or graphics, which may alter content. The journal's standard [Terms & Conditions](#) and the [Ethical guidelines](#) still apply. In no event shall the Royal Society of Chemistry be held responsible for any errors or omissions in this *Accepted Manuscript* or any consequences arising from the use of any information it contains.

# Open-Framework Iron Fluoride and Reduced Graphene Oxide Nanocomposite as a High-Capacity Cathode Material for Na-ion Batteries

Ghulam Ali<sup>a,b</sup>, Si Hyoung Oh<sup>a,b</sup>, Se Young Kim<sup>a</sup>, Ji Young Kim<sup>a</sup>, Byung Won Cho<sup>a</sup> and Kyung Yoon Chung<sup>a,b\*</sup>

<sup>a</sup>*Center for Energy Convergence Research, Korea Institute of Science and Technology, Hwarang-ro 14-gil 5, Seongbuk-gu, Seoul 136-791, Republic of Korea*

<sup>b</sup>*Energy Conversion Technology, Korea University of Science and Technology, 217 Gajeong-ro Yuseong-gu, Daejeon 305-333, Republic of Korea*

\*Corresponding author.

e-mail: [kychung@kist.re.kr](mailto:kychung@kist.re.kr)

Phone number: +82-2-958-5228

Fax number: +82-2-958-5229

## Abstract

Cathode materials with high capacity and good stability for rechargeable Na-ion batteries (NIBs) are few in number. Here, we report a composite of electrochemically active iron fluoride hydrate and reduced graphene oxide (rGO) as a promising cathode material for NIBs. Phase-pure  $\text{FeF}_3 \cdot 0.5\text{H}_2\text{O}$  is synthesized by a non-aqueous precipitation method and a composite with rGO is prepared to enhance the electrical conduction. The encapsulation of  $\text{FeF}_3 \cdot 0.5\text{H}_2\text{O}$  nanoparticles between the rGO layers results in a lightweight and stable electrode with a three-dimensional network. The composite material delivers a substantially enhanced discharge capacity of 266  $\text{mAh g}^{-1}$  compared to 158  $\text{mAh g}^{-1}$  of the bare  $\text{FeF}_3 \cdot 0.5\text{H}_2\text{O}$  at a current density of 0.05 C. This composite also shows a stable cycle performance with a high capacity retention of >86% after 100 cycles, demonstrating its potential as a cathode material for NIBs.

## Introduction

Lithium-ion batteries (LIBs) exhibit limitations in terms of safety and cost,<sup>1</sup> which has prompted the search for alternatives to meet future requirements of energy storage. Sodium has emerged as a prospective charge-carrier material for rechargeable batteries because of its low cost and natural abundance compared to lithium.<sup>2</sup> Sodium is located beneath lithium in the periodic table and the two elements resemble each other in terms of chemical properties. Hence, Na can be a good alternative for lithium, especially for large-scale applications, such as in electric vehicles (EVs) and grid storage. Rechargeable batteries based on metallic sodium anodes have lower operating voltage, gravimetric capacity, and energy density compared to LIBs, making them less competitive.<sup>3-9</sup> The most important factor determining the use of a material for large-scale

applications, such as energy-storage systems (ESS) is cost, while energy density is a less serious issue.<sup>10</sup> Na-ion batteries (NIBs) are now strong candidates for large-scale applications.

Intercalated layered cathode materials, such as  $\text{Na}_x\text{MO}_2$  ( $\text{M}$  = transition metal) in NIBs have already been explored; however, their reversible capacities ( $100\text{--}120\text{ mAh g}^{-1}$ ) are limited.<sup>1</sup> NIBs rely mainly on intercalated metal-oxide cathode materials, which place restrictions on their large-scale applications because of the use of costly cobalt, nickel, and vanadium-based materials, which also pose environmental issues. Moreover, the moderate energy densities of these materials make them unsuitable for high-power applications in ESS and HEVs.<sup>11</sup> Fluoride-based materials however, are competitive alternatives as NIB cathode materials because a number of trifluorides operate at high voltages because of their high electronegativity. The other advantage of these materials is their high theoretical capacities ( $500\text{--}750\text{ mAh g}^{-1}$  for many transition-metal fluorides), which is favorable for obtaining electrodes with high experimental capacities.<sup>12, 13</sup> As most metal fluorides have open structures for transportation of alkali ions, these materials suffer from the drawback of poor reaction kinetics because of their low electronic conductivities resulting from the ionic nature of metal–fluorine bonding.<sup>14</sup> To improve their conductivity, different kinds of carbonaceous materials, such as acetylene black,<sup>15</sup> graphite,<sup>16</sup> single-walled carbon nanotubes,<sup>17</sup> activated carbon microbeads,<sup>18</sup> and graphene<sup>19</sup> are used to form composites with the active materials. Incorporating the rGO as conductive additive for composite electrode is an efficient approach to achieve stable cycling and high-rate capability as rGO offers high specific surface area and excellent electrical conductivity. Graphene sheets can serve as electrical contacts between the particles of active material and leading to excellent electrochemical performance of the electrode.<sup>20</sup> Among metal fluorides, iron fluoride ( $\text{FeF}_3$ ), with its high theoretical capacity of  $712\text{ mAh g}^{-1}$  (with three electron transfer), is an appealing cathode

material for LIBs.<sup>21</sup> Due to high ionicity,  $\text{FeF}_3$  operates at high potentials and considered as next-generation electrode for rechargeable batteries.<sup>22</sup> Considerable research has been devoted to explore the reaction mechanism of  $\text{FeF}_3$  cathode in LIBs.<sup>23, 24</sup> However, there are only a few reports on using iron fluorides as NIB cathode materials.<sup>25, 26</sup>

Here, we prepared a composite of iron fluoride hydrate ( $\text{FeF}_3 \cdot 0.5\text{H}_2\text{O}$ ) and reduced graphene oxide (rGO), referred to as  $\text{FeF}_3 \cdot 0.5\text{H}_2\text{O}$ -rGO hereafter, and demonstrated its use as a NIB cathode material. The theoretical capacity of  $\text{FeF}_3 \cdot 0.5\text{H}_2\text{O}$  is  $220 \text{ mAh g}^{-1}$  (with one cycle of Na insertion) and the working voltage is  $\sim 3 \text{ V}$  against Li.<sup>27</sup> In this work, rGO was used to enhance the electrical conduction paths in  $\text{FeF}_3 \cdot 0.5\text{H}_2\text{O}$  particles and thus decrease the polarization effects. Microscopic measurements clearly indicate good adhesion between the rGO layers and the  $\text{FeF}_3 \cdot 0.5\text{H}_2\text{O}$  nanoparticles. The bare material exhibited a discharge capacity of  $158 \text{ mAh g}^{-1}$  against sodium, while the composite material delivered an extraordinary discharge capacity of  $266 \text{ mAh g}^{-1}$  with a good cycle life. The better electrochemical performance of the composite electrode is attributed to the interactions between the  $\text{FeF}_3 \cdot 0.5\text{H}_2\text{O}$  nanoparticles and rGO sheets.

## Results and discussion

The use of an ionic liquid, 1-butyl-3-methylimidazolium tetrafluoroborate ( $\text{BMIM}[\text{BF}_4]$ ), as the fluorine source provided a simple architecture to produce  $\text{FeF}_3 \cdot 0.5\text{H}_2\text{O}$  nanoparticles and the  $\text{FeF}_3 \cdot 0.5\text{H}_2\text{O}$ -rGO composite. As a reaction medium, the ionic liquid, in addition to dissolving the starting material, also provided  $\text{F}^-$  ions, which reacted with the  $\text{Fe}^{3+}$  ions to produce the final product (the water content in the structure could be lowered by controlling the chemical reaction in vacuum).<sup>28</sup> This low-temperature and ambient-pressure synthesis environment led to the formation of phase-pure bare  $\text{FeF}_3 \cdot 0.5\text{H}_2\text{O}$  and  $\text{FeF}_3 \cdot 0.5\text{H}_2\text{O}$ -rGO.

The X-ray diffraction (XRD) patterns of the bare material and their Rietveld-refinement results (Fig. 1a) show that the crystal structure can be indexed to the cubic  $Fd-3m$  space group. The lattice parameter was calculated to be  $a = 10.407 \text{ \AA}$ . The crystal structure of  $\text{FeF}_3 \cdot 0.5\text{H}_2\text{O}$  is regarded as a ‘hydrated version’ of the  $\text{FeF}_3$  pyrochlore reported by Ferey et al.<sup>29</sup> In general, a pyrochlore has the chemical formula  $\text{A}_2\text{B}_2\text{X}_6\text{Z}_{1-\delta}$ , where A is an eight-coordinated cation with a large size and the B site is occupied by a six-coordinated cation with a high charge. Anions, such as O and F occupy the X and Z sites, while  $\text{H}_2\text{O}$  or vacancies can also occupy Z sites. The  $\text{FeF}_3$  pyrochlore is isostructural with  $\text{B}_2\text{X}_6$  in the general pyrochlore, where the corner-sharing  $\text{BX}_6$  octahedra generate a cage-like framework and the  $\text{A}_2\text{Z}$  unit is absent. We assume that  $\text{FeF}_3$  in the  $\text{FeF}_3 \cdot 0.5\text{H}_2\text{O}$  prepared in the current study had the same structure as  $\text{B}_2\text{X}_6$ , while  $\text{H}_2\text{O}$  occupied the Z position and A was absent in  $\text{A}_2\text{B}_2\text{X}_6\text{Z}_{1-\delta}$ . As shown in Fig. 1b,  $\text{H}_2\text{O}$  was located at the center of each cage made of the  $\text{FeF}_6$  octahedra. The unit cell volume of  $\text{FeF}_3 \cdot 0.5\text{H}_2\text{O}$  ( $1127.4 \text{ \AA}^3$ ) was larger than that of the  $\text{FeF}_3$  pyrochlore ( $1100.7 \text{ \AA}^3$ ) probably because of the presence of water molecules in the pyrochlore structure. A large three-dimensional open framework is favorable to the  $\text{Na}^+$ -insertion electrochemistry. Other structural information related to the refinement is summarized in Tables S1 and S2 (supplementary material). In the XRD pattern and pattern refinement of the  $\text{FeF}_3 \cdot 0.5\text{H}_2\text{O}$ -rGO composite (Fig. 1c), a less intense broad rGO peak appears in the  $2\theta$  range of  $22-26^\circ$ . The bare sample also contained carbon, which probably originated from the residue of the ionic liquid in the final product and was not detected by XRD. The carbon content, measured by C/S elemental analysis, was  $\sim 1.1 \text{ wt\%}$  in the bare sample and  $\sim 13 \text{ wt\%}$  in the composite.

The removal of hydration from bare  $\text{FeF}_3 \cdot 0.5\text{H}_2\text{O}$  was carried out during thermogravimetric analysis (TGA). Three different temperature regions can be observed in the

results shown in Fig. 2a. The first region, up to 235 °C, shows the removal of adsorbed water and any organic contents from the surface, while the material structure remained unchanged. The second region between the two high derivative peaks at 236 and 314 °C can be attributed to the complete removal of ~7.4% of bonded water from  $\text{FeF}_3 \cdot 0.5\text{H}_2\text{O}$ . The material structure was also deformed by the removal of hydrate content, as confirmed by temperature-dependent time-resolved XRD results (Fig. 2b). The third region from 315 to 497 °C can be attributed to the formation of new phases. Thermal analysis of  $\text{FeF}_3 \cdot 0.5\text{H}_2\text{O}$  revealed that the material was only stable as long as water remained in the structure. The total weight loss was 40.5% when heated from room temperature to 497 °C; the material was completely transformed and  $\text{Fe}_2\text{O}_3$  was the new phase detected at this temperature. Further detail of structural transformation is enclosed in supporting information.

The morphology of bare  $\text{FeF}_3 \cdot 0.5\text{H}_2\text{O}$  was characterized by scanning electron microscopy (SEM) and transmission electron microscopy (TEM). The SEM images in Fig. 3a and b show the formation of large spherical particles, referred to as nanoballs hereafter, which were uniform in both shape and size. These nanoballs with diameters of ~400 nm were composed of primary nanoparticles of variable sizes (5–15 nm), which can be observed at higher magnification (inset of Fig. 3b). The primary nanoparticles are gathered with intermediate voids between them and give rise to the mesoporosity which is in favor of even diffusion of electrolyte. The Brunauer–Emmett–Teller (BET) surface area (Supplementary Fig. S1a) of these mesoporous particles was  $42 \text{ m}^2 \text{ g}^{-1}$ , and the adsorption data was in the form of a type IV isotherm. The pore-size distribution curve for the bare material (the inset of Supplementary Fig. S1a) displays a peak centred at ~3.7 nm. The TEM image in Fig. 3c shows primary nanoparticles agglomerated to each other to form big nanoballs which offer high surface area in contact with the electrolyte and

expected to promote  $\text{Na}^+$  insertion–extraction. The SEM image in Fig. 3d shows a vertical view of the typical contiguity locus of  $\text{FeF}_3 \cdot 0.5\text{H}_2\text{O}$  particles and rGO layers. Most of the  $\text{FeF}_3 \cdot 0.5\text{H}_2\text{O}$  particles were well attached and confined within the rGO sheets to form a three-dimensional network, enabling rapid electrical conduction. Since the rGO comprised of several layers, the  $\text{FeF}_3 \cdot 0.5\text{H}_2\text{O}$ –rGO composite exhibited high porosity, which is favorable for ion transport and electrolyte penetration. The SEM image at higher magnification (Fig. 3e) shows the growth of spherical particles with almost the same size as that in the bare material. The TEM image of the composite in Fig. 3f shows very small particles with sizes ranging from 10 to 50 nm scattered onto that rGO layers, which were not detected by the SEM.

The cells were galvanostatically cycled at room temperature and a constant current–constant voltage mode was applied during charging (to 4.5 V). Figure 4a shows the charge–discharge profile of bare  $\text{FeF}_3 \cdot 0.5\text{H}_2\text{O}$  against Na metal in the range 1.5–4.5 V. The bare material delivered a discharge capacity of  $121 \text{ mAh g}^{-1}$  at a current density of 0.05 C in the first cycle ( $1 \text{ C} = 220 \text{ mAh g}^{-1}$ ). In the initial cycles, the material delivered a low discharge capacity and showed a plateau at  $\sim 1.9 \text{ V}$ . The discharge capacity increased in subsequent cycles and reached a maximum of  $158 \text{ mAh g}^{-1}$ , with an additional significant voltage plateau at  $\sim 2.8 \text{ V}$ . This voltage of  $\text{FeF}_3 \cdot 0.5\text{H}_2\text{O}$  in NIBs is roughly 0.2 V lower than the corresponding value in LIBs. It also agrees well with the ab initio calculations, which show that Na insertion reduces the potential by 0.18–0.57 V compared to Li insertion in the compounds.<sup>30</sup> Figure 4a shows a large gap between the charging and discharging curves, which indicates high polarization, intrinsic to fluoride-based materials as they exhibit a larger difference than  $\sim 1.1 \text{ V}$  in charge–discharge curves.<sup>31</sup> Fig. 4b shows the cyclic voltammograms of bare  $\text{FeF}_3 \cdot 0.5\text{H}_2\text{O}$  at a scan rate of  $0.2 \text{ mV s}^{-1}$  between 1.5 and 4.5 V. In the first cycle of the cathodic process, there was only one

significant reduction peak at around 2 V, but another peak at  $\sim 2.74$  V was observed in the second cycle. During the anodic process, a broad oxidation peak was observed at  $\sim 2.55$  V. The discharge profile of the bare material (Fig. 4c) shows capacities of 128, 93, 59, and 36 mAh g<sup>-1</sup> at higher current densities of 0.1, 0.25, 0.5, and 1 C, respectively. The inset of Fig. 4c shows the discharge capacities of the bare material at different current rates versus the number of cycles. When the current density was reset to 0.05 C after deep cycling, the discharge capacity not only recovered but also was slightly higher than the initial capacities and the recorded value for the final cycle was 184 mAh g<sup>-1</sup>. This high capacity can probably be attributed to the increase in the activation of the material with cycling. These results illustrate the good stability and tolerance of bare FeF<sub>3</sub>·0.5H<sub>2</sub>O for Na<sup>+</sup> insertion–extraction.

Compared to the bare material, the FeF<sub>3</sub>·0.5H<sub>2</sub>O–rGO composite delivered a higher capacity. Fig. 5a shows the charge–discharge profile of the composite material in the 1.5–4.5 V range. In the first cycle, the discharge capacity was as high as 239 mAh g<sup>-1</sup> at a current density of 0.05 C. The discharge capacity reached a maximum of 266 mAh g<sup>-1</sup> in the 6<sup>th</sup> cycle with a noticeable plateau at 2.8 V, indicating that 21% more Na ions than the theoretical capacity (220 mAh g<sup>-1</sup> with one sodium ion) were inserted in the active material. The better electrochemical performance of the composite is also attributed to the unique growth of the active material with nanometer sized particles attached to the rGO layers with a high specific area of 155 m<sup>2</sup> g<sup>-1</sup>, which is 3.7 times that of the bare material (Fig. S1b in supporting information). These rGO layers facilitated electron transport to the surface of the active material to a larger extent, thus providing Na<sup>+</sup> ions with efficient access into the structure. Electrochemical impedance spectroscopic results show that the charge transfer resistance is much lowered in composite (110 Ω) as compare to the bare electrode (306 Ω), shown in Fig. S2 (supporting information). The

cyclic voltammograms of the composite material (in the range 1.5–4.5 V at a scan rate of 0.2 mV s<sup>-1</sup>, Fig. 5b) show a peak at ~2.7 V in the second cycle of the cathodic reaction. On the other hand, no significant sharp peak was recorded during the anodic reaction in the initial cycles, but a broad peak can be seen in the voltammograms in the 2.6–3.2 V region. In the graphs of discharge capacities at different current rates (Fig. 5c), the shape of the initial charge–discharge curve remains almost unchanged at higher current densities of 0.1 and 0.25 C; the respective discharge capacities of 190 and 153 mAh g<sup>-1</sup> demonstrate the good rate capability of the composite. However, the discharge capacity decreased to 90 mAh g<sup>-1</sup> and 64 mAh g<sup>-1</sup> at higher current densities of 0.5 and 1 C, respectively, showing relatively rapid fading in the capacity. It is worth mentioning here that all the cells were galvanostatically cycled five times in the range 1.0–4.5 V at a current density of 0.05 C prior to any measurement.

In order to determine the contribution of capacity from rGO, rGO electrodes were prepared under experimental conditions identical to that used for the bare and composite material. Surprisingly, the rGO electrode delivers a discharged capacity of 78 mAh g<sup>-1</sup> at a 0.05 C-rate in the voltage range 1.5–4.5 V, as shown in Fig. 6. The amount of rGO is ~13 wt% in the composite; hence, it would contribute only about 10 mAh g<sup>-1</sup> to the overall electrode capacity.

Cycle performance is an essential parameter of electrode materials for long-term application. Fig. 7a shows the cycling behavior of the bare and composite materials at a constant current rate of 0.05 C in the range 1.5–4.5 V (versus Na/Na<sup>+</sup>). The initial discharge capacities of the bare and composite electrodes were 151 and 242 mAh g<sup>-1</sup>, respectively. The bare material delivered a slightly decreased discharge capacity of 135 mAh g<sup>-1</sup> after 80 cycles, indicating good cycle stability of the material. The composite material exhibited a high discharge capacity of 230 mAh g<sup>-1</sup> after 100 cycles, suggesting that the Na<sup>+</sup> insertion–extraction process was quite

reversible. The plateaus in Fig. 7b also becomes more pronounced with cycling, signifying the high energy density of the material. The good cycling stability shows that the composite is a promising cathode material for NIBs.

To monitor the structural mechanism in more detail, ex situ TEM and X-ray absorption near-edge structure (XANES) spectroscopy were employed to explore the electrochemical reaction. Fig. 8 shows the TEM images and XANES spectra of pristine  $\text{FeF}_3 \cdot 0.5\text{H}_2\text{O}$ -rGO and samples discharged to 2.0 and 1.5 V, recharged to 4.2 and 4.5 V. Fig. 8a shows the selected area diffraction (SAD) pattern of the pristine sample. The measured  $d$ -spacing and their corresponding reflections in  $\text{FeF}_3 \cdot 0.5\text{H}_2\text{O}$  are matched with the XRD pattern in Fig. 1a. The high-resolution TEM (HR-TEM) image and SAD pattern of the sample discharged to 2.0 V is shown in Fig. 8b. The measured values of the  $d$ -spacing, as acquired from the lattice fringes in the HR-TEM image, show the formation of NaF at the edges of the sphere. The intense rings observed in the SAD pattern (inset of Fig. 8b) were acquired from the same area and are associated with NaF (002) and Fe (111) phases. The same products have been found in the sample discharged to 1.5 V. HR-TEM images show that the host structure transforms to an amorphous-like phase (most of the part of the particles) and the host structure also reacts with  $\text{Na}^+$  to produce NaF and Fe converted phases. This shows the conversion reaction to some extent in the material. During charging, NaF and Fe have been found until 4.2 V; however, these were not detected when the sample charged to 4.5 V. In this sample, the reflection (222) peak corresponds to  $\text{FeF}_3$  (ICSD#98-020-2047). This shows the partially reversible conversion reaction of the material at the edges of the particles. Atomic weight percent (with  $\pm 2$  wt% accuracy) of the various elements determined from energy-dispersive X-ray (EDX) analysis is shown in Table S4 (supplementary information). Even in the sample fully charged to 4.5 V, Na

atoms cannot be completely extracted and the electrode contains 5.21 wt% Na. High resolution TEM image of fully charged composite electrode is also taken after 100 galvanostatic cycles as shown in Fig. 8f. The particles preserved their shape and size even after long cycling as shown in Fig. S3 (supporting information), however, they show amorphous-like phase. A poor crystalline behavior can be observed at the edge of the particle and the rings in the SAD pattern (inset of Fig. 8f) can be indexed to Fe (ICSD#98-004-1506) and  $\text{FeF}_3$  phases.

Ex situ XANES measurements were then performed at the Fe K-edge to examine the oxidation/reduction of Fe upon electrochemical Na intercalation or de-intercalation in the  $\text{FeF}_3 \cdot 0.5\text{H}_2\text{O}$ -rGO composite. Fig. 9a shows a significant shift towards lower energy among the Fe K-edge XANES spectra of the partially discharged materials, which, as expected, is consistent with the reduction reaction mechanism occurring upon insertion of  $\text{Na}^+$  ions in the host structure. For the composite discharged to 2.0 V, the main-edge peak is significantly farther from that observed in the pristine sample and its shift in energy can be observed more clearly in the first derivative shown in Fig. 9b. Upon further discharging of the composite to 1.5 V, the obtained spectrum shows a shift towards lower energy, a sign of further reduction of Fe in the  $\text{FeF}_3 \cdot 0.5\text{H}_2\text{O}$ -rGO composite. This confirms that the electrochemical reaction and capacity of the composite were mainly due to the reduction of Fe ions. The main-edge feature is shifted towards higher energy in the spectrum obtained after  $\text{Na}^+$  extraction, showing that oxidation occurred, and the spectrum is lowered in energy compared to that of the pristine composite charged to 4.5 V. The spectrum of the sample fully charged to 4.5 V differs in shape and position with the  $\text{FeF}_3 \cdot 0.5\text{H}_2\text{O}$ -rGO, indicating the changes in the local arrangement of neighboring atoms and the oxidation state of the central atom.<sup>32</sup> The spectra also shows isosbestic point at 7156 eV (marked with dotted circle), indicating the transformation of phases during oxidation-

reduction reaction. For comparison, the spectra from  $\text{FeF}_2$  and  $\text{FeF}_3$  were also measured. The pristine samples were almost similar in energy as  $\text{FeF}_3$ , whereas the sample fully discharged to 1.5 V shows higher energies than  $\text{FeF}_2$ , indicating that the overall oxidation state of Fe remains  $>2+$ .

In summary, the capacities of the NIB cathodes are substantially improved in comparison to the performance of  $\text{FeF}_3 \cdot 0.5\text{H}_2\text{O}$  cathodes (which delivered a capacity of  $135 \text{ mAh g}^{-1}$ ) in LIBs<sup>27</sup> and the nanostructured  $\text{FeF}_3 \cdot 0.5\text{H}_2\text{O}$ -rGO composite delivered a high discharge capacity of  $266 \text{ mAh g}^{-1}$ , which is almost twice that of  $\text{FeF}_3 \cdot 0.33\text{H}_2\text{O}$ ,  $130 \text{ mAh g}^{-1}$  in the range 1.2–4.0 V.<sup>33</sup> The capacity of the composites reported in this study is also higher than that of anhydrate iron fluoride compounds, such as  $\text{NaFeF}_3$  and  $\text{FeF}_3$ -C composites<sup>14, 26</sup> ( $170$  and  $100 \text{ mAh g}^{-1}$ , respectively, with a limited cyclability). The composite material exhibited a high capacity of  $266 \text{ mAh g}^{-1}$ , which is 20% higher than the theoretical capacity ( $220 \text{ mAh g}^{-1}$  for one  $\text{Na}^+$ ). A detailed study has been conducted to explore the electrochemical performance of the  $\text{FeF}_3 \cdot 0.5\text{H}_2\text{O}$ -rGO composite and its reaction mechanism was studied via TEM and XANES. This study shows that the extra capacity partially arose from rGO ( $\sim 10 \text{ mAh g}^{-1}$ ) and the conversion reaction at the edges of the particles, where  $\text{Fe}^{3+}$  reduces to  $\text{Fe}^0$  contributed to the rest. This conversion reaction is evidenced from the ex situ TEM images during discharging where converged products ( $\text{NaF}$  and  $\text{Fe}$ ) are detected. To further confirm the extent of this conversion reaction, ex situ XANES analysis is performed and the overall oxidation state of Fe remains  $<2+$  upon discharging to 1.5 V. Ex situ TEM and XANES analysis indicated that if the upper cut-off voltage limit was lower than 4.5 V, the material showed irreversibility.

## Conclusions

The feasibility of the use of iron fluoride hydrate  $\text{FeF}_3 \cdot 0.5\text{H}_2\text{O}$  as a high-performance cathode material in Na-ion batteries was investigated. We prepared a  $\text{FeF}_3 \cdot 0.5\text{H}_2\text{O}$ -rGO nanocomposite with morphological advantages, where  $\text{FeF}_3 \cdot 0.5\text{H}_2\text{O}$  particles were encapsulated in rGO sheets, allowing for excellent ion transport, and the large surface area of the composite provided an enhanced electrochemical activity because of the higher contact between the particle surface and electrolyte. The composite exhibited an enhanced discharge capacity of  $266 \text{ mAh g}^{-1}$  compared to  $158 \text{ mAh g}^{-1}$  of the bare  $\text{FeF}_3 \cdot 0.5\text{H}_2\text{O}$  at  $0.05 \text{ C}$ . Furthermore, both bare and composite materials exhibited a good cycle life and a small capacity decay of the composite occurred after 100 cycles. Owing to the polarization effects and large ionic size of Na, the high rate capability of the material (at  $>1 \text{ C}$ ) was not appreciably enhanced and further modifications in the structure and coating processes are required. The electrochemical reaction mechanism of composite was explored using ex situ TEM, which show the diversification of the material into different phases. The material transformed in to amorphous-like phase, whereas it also showed a conversion reaction on the edges of the particles upon cycling. This diversification of the material along with superior morphology (three-dimensional network) could be the reason for the high capacity of the composite. The XANES spectra of the  $\text{FeF}_3 \cdot 0.5\text{H}_2\text{O}$ -rGO composite provided valuable information on the electrochemical reaction occurring through the reduction (oxidation) of iron. We believe that these results will exert a profound impact on the development of high-capacity cathode materials for NIBs in large-scale applications.

## **Experimental section**

### **Material synthesis**

An ionic liquid, BMIM[BF<sub>4</sub>] (> 98%, Aldrich), was used as the fluorine source and Fe(NO<sub>3</sub>)<sub>3</sub>·9H<sub>2</sub>O (99.99%, Aldrich) was the source of iron and hydration content for the final product. The iron fluoride hydrate (FeF<sub>3</sub>·0.5H<sub>2</sub>O) was prepared by a non-aqueous precipitation method reported elsewhere.<sup>17</sup> Graphite oxide was prepared by Hummer's method and then reduced at 700 °C for 5 h in nitrogen atmosphere to obtain the final product for further processing.<sup>34</sup> In a typical synthesis of the composite material, rGO was mixed with 12.1 g of BMIM[BF<sub>4</sub>] and magnetically stirred for 1 h to achieve a homogeneous dispersion. Then, 1 g of iron nitrate was added slowly into the solution and on complete dissolution the solution was moved to vacuum for 2 h to evaporate the excess water content. The solution was agitated again for 14 h at 50 °C to form the precipitates. The material was collected after centrifugation at 5000 rpm and washed with acetone several times to remove the residual ionic liquid and nitrate impurities. The material was then dried under vacuum at 80 °C overnight prior to the structural and other characterization. The bare material was produced following the same procedure, without the addition of rGO.

**Characterization.** XRD patterns of bare FeF<sub>3</sub>·0.5H<sub>2</sub>O and the FeF<sub>3</sub>·0.5H<sub>2</sub>O–rGO composite were obtained using powder X-ray diffraction (XRD) at the 9B-HRPD beamline at Pohang Light Source (PLS, Korea), a third-generation synchrotron radiation source. Synchrotron XRD of the samples was recorded with six base detectors using a step size of 0.01°, exposure time of 4 s, and 2θ range 10–90°. The thermal behavior of FeF<sub>3</sub>·0.5H<sub>2</sub>O under an inert nitrogen atmosphere was studied using a thermogravimetric analyzer (SDT-Q600, TA Instruments, USA) between room temperature and 600 °C at a constant heating rate of 5 °C min<sup>-1</sup>. Temperature-dependent time-resolved XRD was obtained using a diffractometer at Korea Institute of Science and Technology

(KIST) and the operation conditions are supplied in supplementary information along with its product phases. The morphologies of bare  $\text{FeF}_3 \cdot 0.5\text{H}_2\text{O}$  and the  $\text{FeF}_3 \cdot 0.5\text{H}_2\text{O}$ -rGO composite were determined with field-emission scanning electron microscopy (FE-SEM; NOVA NanoSEM200, FEI, USA). High-resolution transmission electron microscopy (Tecnai G<sup>2</sup> F20, FEI) was used to observe the particle morphology of the bare  $\text{FeF}_3 \cdot 0.5\text{H}_2\text{O}$  and  $\text{FeF}_3 \cdot 0.5\text{H}_2\text{O}$ -rGO composite.

Ex situ TEM and X-ray absorption near-edge structure (XANES) spectroscopy were employed to determine the electrochemical reaction mechanism. For the sample preparation, the cells were disassembled at different charged and discharged states in an argon-filled glove box. The electrodes were collected and thoroughly washed with a dimethyl carbonate (DMC) to remove any residual electrolyte. For ex situ TEM, the material was gently scratched from the Al foil, sonicated in DMC and dropped onto carbon TEM grid. Ex situ XANES spectroscopy was employed to determine the oxidation state of Fe and structural changes at different potentials of composite material. The XANES measurements of the electrodes were performed at the 1D beamline in the 2.5-GeV Pohang Light Source (ring current of 120–160 mA). The Fe K-edge X-ray absorption spectroscopy (XAS) data were acquired in the total-electron-yield mode and the sample current was recorded. Ion chamber detectors filled with high-purity nitrogen were used to record the X-ray absorption spectra.  $\text{FeF}_2$  (Aldrich) and  $\text{FeF}_3$  (Aldrich) were used for comparison to analyze the samples.

**Electrochemical tests.** To prepare the electrodes for electrochemical tests, the bare and composite samples were mixed with carbon black and polyvinylidene difluoride (PVdF) in a weight ratio of 7:1.5:1.5. *N*-methyl-2-pyrrolidone was added to the above mixture until a

homogeneous viscosity was obtained. The mixture was cast onto Al foil, dried at 80 °C for 4 h, and then roll-pressed to produce the electrodes for electrochemical testing. The electrodes were vacuum dried at 80 °C overnight before cell assembly.

Galvanostatic measurements were performed using CR 2032 type coin cells with bare  $\text{FeF}_3 \cdot 0.5\text{H}_2\text{O}$  and the  $\text{FeF}_3 \cdot 0.5\text{H}_2\text{O}$ -rGO composite as working electrodes, a polypropylene separator, and sodium metal (Aldrich, 99.9%) as the counter electrode. The thickness of the working electrodes was  $\sim 30 \mu\text{m}$  and the average mass loading of the bare and composite electrodes were 1.4 and  $0.85 \text{ mg cm}^{-2}$ , respectively. A mixture of 1 M  $\text{NaClO}_4$  in propylene carbonate, ethylene carbonate, and diethyl carbonate in a ratio of 1:1:1 was used as the electrolyte. Galvanostatic tests were carried out with a battery cycler (Maccor 4000, USA) linked to a computer. The cell fabrication was carried out in an argon-filled glove box (MBRAUN UNIlab, Germany) with less than 0.1 ppm of  $\text{H}_2\text{O}$  and  $\text{O}_2$ .

### **Additional information**

Electronic supplementary information (ESI) is available in the online version of the paper. Reprints and permissions information is available online at [www.rsc.org/MaterialsA](http://www.rsc.org/MaterialsA). Correspondence and requests for materials should be addressed to K.Y.C.

### Figure captions

**Fig. 1.** (a) Powder XRD pattern of bare  $\text{FeF}_3 \cdot 0.5\text{H}_2\text{O}$  and its Rietveld refinement. (b) Schematic representation of  $\text{FeF}_3 \cdot 0.5\text{H}_2\text{O}$ ; the crystal structure is cubic pyrochlore with space group  $Fd-3m$ . (c) Powder XRD of the  $\text{FeF}_3 \cdot 0.5\text{H}_2\text{O}$ -rGO composite and its Rietveld refinement.

**Fig. 2.** (a) Thermogravimetric analysis data and (b) Temperature-dependent time-resolved XRD of bare  $\text{FeF}_3 \cdot 0.5\text{H}_2\text{O}$ .

**Fig. 3.** (a) Low-magnification SEM image of bare  $\text{FeF}_3 \cdot 0.5\text{H}_2\text{O}$  showing the growth of particles into spherical shapes. (b) High-magnification SEM image of bare  $\text{FeF}_3 \cdot 0.5\text{H}_2\text{O}$ ; the inset shows tiny nanoparticles from a single sphere. (c) TEM image of bare  $\text{FeF}_3 \cdot 0.5\text{H}_2\text{O}$  showing a single sphere composed of tiny nanoparticles. SEM images of  $\text{FeF}_3 \cdot 0.5\text{H}_2\text{O}$ -rGO composite at (d) low and (e) high magnification. (f) TEM image of  $\text{FeF}_3 \cdot 0.5\text{H}_2\text{O}$ -rGO showing the contacts between particles and the rGO layer.

**Fig. 4.** (a) Galvanostatic charge-discharge voltage profile of the 1<sup>st</sup>, 2<sup>nd</sup> and 10<sup>th</sup> cycle of bare  $\text{FeF}_3 \cdot 0.5\text{H}_2\text{O}$ . (b) Cyclic voltammograms of the bare material between 1.5 and 4.5 V at a scanning rate of  $0.2 \text{ mV s}^{-1}$ . (c) Discharge voltage profile of bare  $\text{FeF}_3 \cdot 0.5\text{H}_2\text{O}$  at various C-rates from 0.05 to 1 C. The inset shows the discharge capacity versus the number of cycles at current rates of 0.05, 0.1, 0.25, 0.5, and 1 C.

**Fig. 5.** (a) Charge-discharge curves of the 1<sup>st</sup>, 2<sup>nd</sup> and 10<sup>th</sup> cycles of the  $\text{FeF}_3 \cdot 0.5\text{H}_2\text{O}$ -rGO composite. (b) Cyclic voltammograms of the composite material between 1.5 and 4.5 V at a scanning rate of  $0.2 \text{ mV s}^{-1}$ . (c) Rate capability of the  $\text{FeF}_3 \cdot 0.5\text{H}_2\text{O}$ -rGO composite at varying current rates from 0.05 to 1 C. The inset shows the discharge capacity versus the number of cycles at current rates of 0.05, 0.1, 0.25, 0.5, and 1 C.

**Fig. 6.** Charge-discharge curves of the rGO electrode and the inset shows the discharge capacity versus cycle number.

**Fig. 7.** (a) Cycle performance of bare  $\text{FeF}_3 \cdot 0.5\text{H}_2\text{O}$  and  $\text{FeF}_3 \cdot 0.5\text{H}_2\text{O}$ -rGO electrodes at a constant current rate of 0.05 C. (b) Discharge profile of 1<sup>st</sup> and end cycle of both bare (plotted with black colored lines) and composite electrode (plotted with red colored lines).

**Fig. 8.** Ex situ high resolution TEM images of (a) pristine  $\text{FeF}_3 \cdot 0.5\text{H}_2\text{O}$ -rGO (b) discharged to 2.0 V (c) discharged to 1.5 V (d) charged to 4.2 V (e) charged to 4.5 V. (f) High resolution TEM image of fully charged  $\text{FeF}_3 \cdot 0.5\text{H}_2\text{O}$ -rGO electrode after 100 cycles.

**Fig. 9.** (a) Ex situ XANES spectra of the Fe K-edge of the  $\text{FeFe}_3$ ,  $\text{FeF}_2$ , pristine  $\text{FeF}_3 \cdot 0.5\text{H}_2\text{O}$ -rGO composite sample, samples discharged to 2.0 and 1.5 V, and samples charged to 4.2 and 4.5 V. (b) The first derivative of XANES spectra.

## Figures

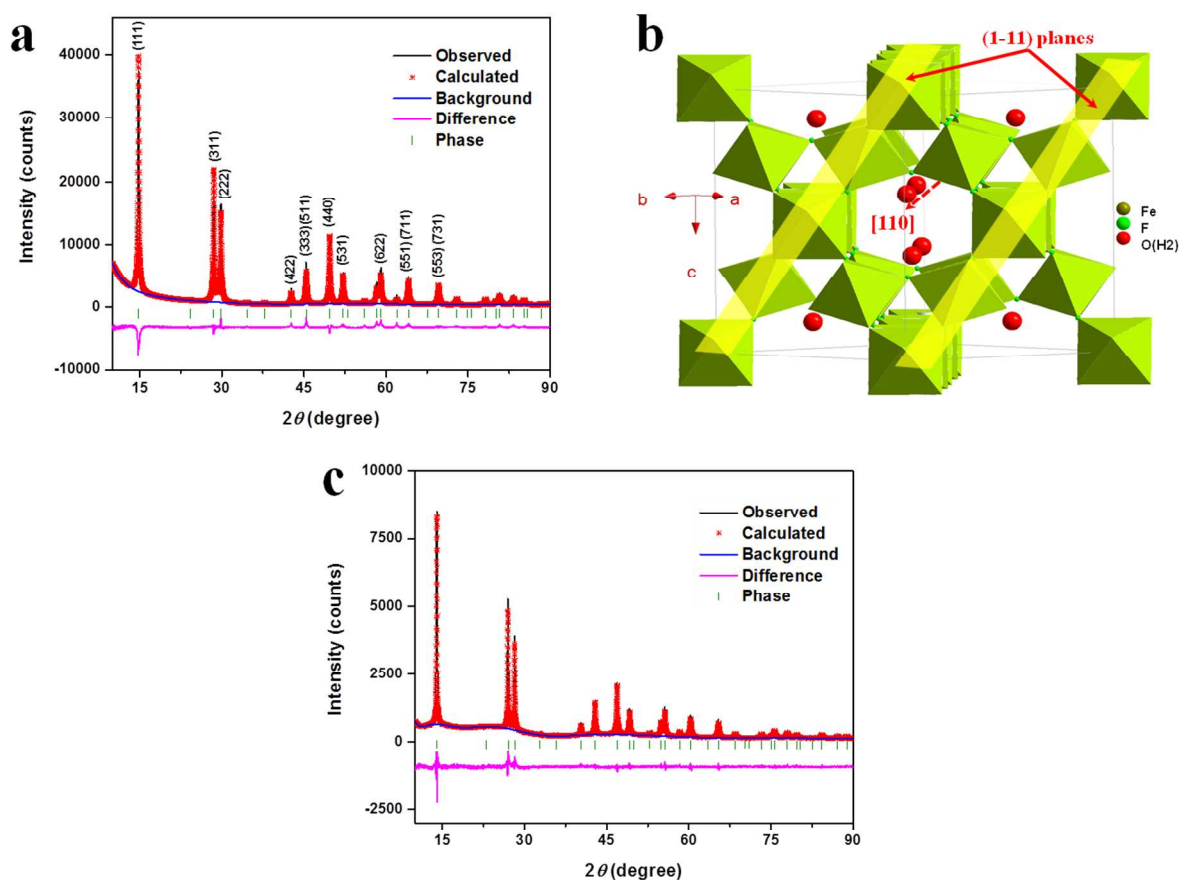


**Figure 1**

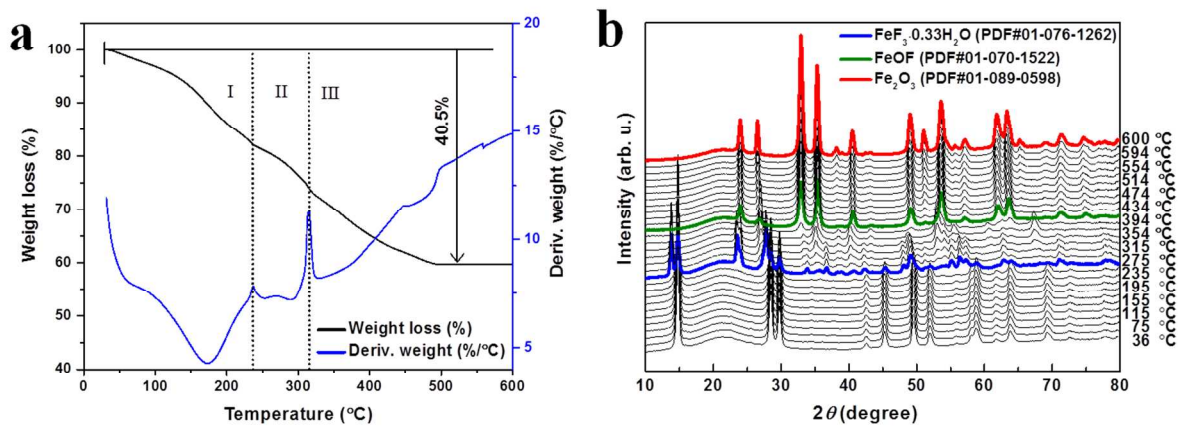
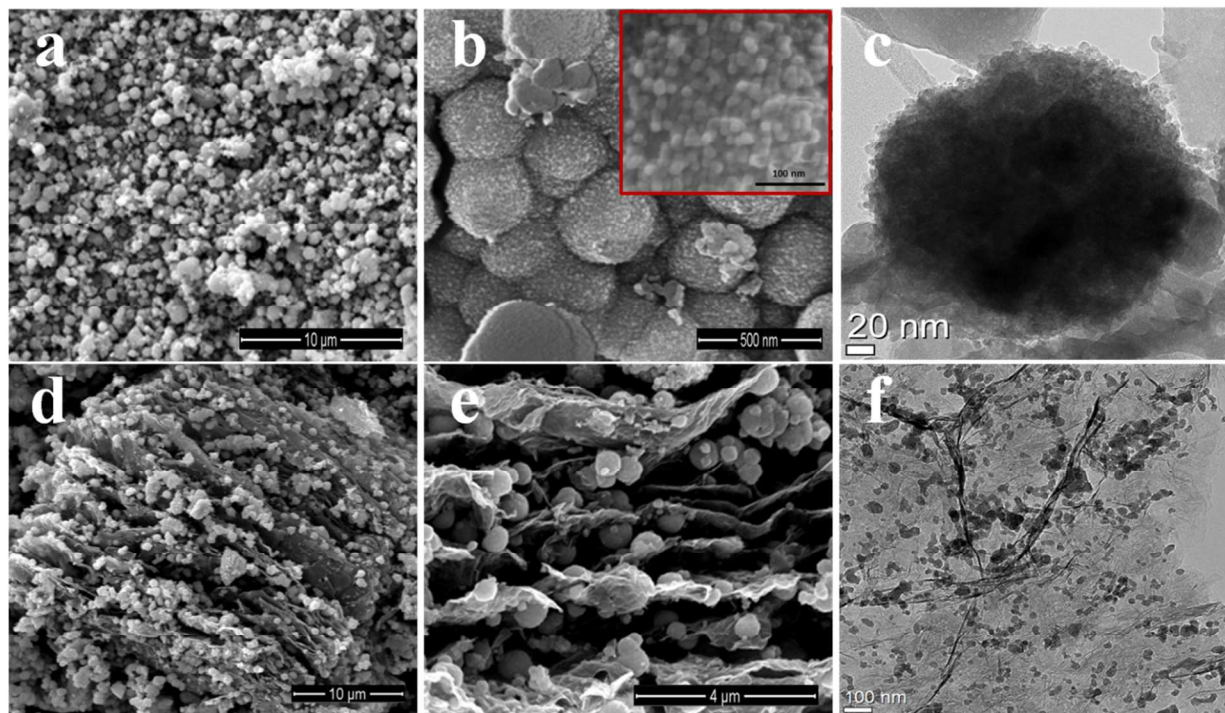


Figure 2



**Figure 3**

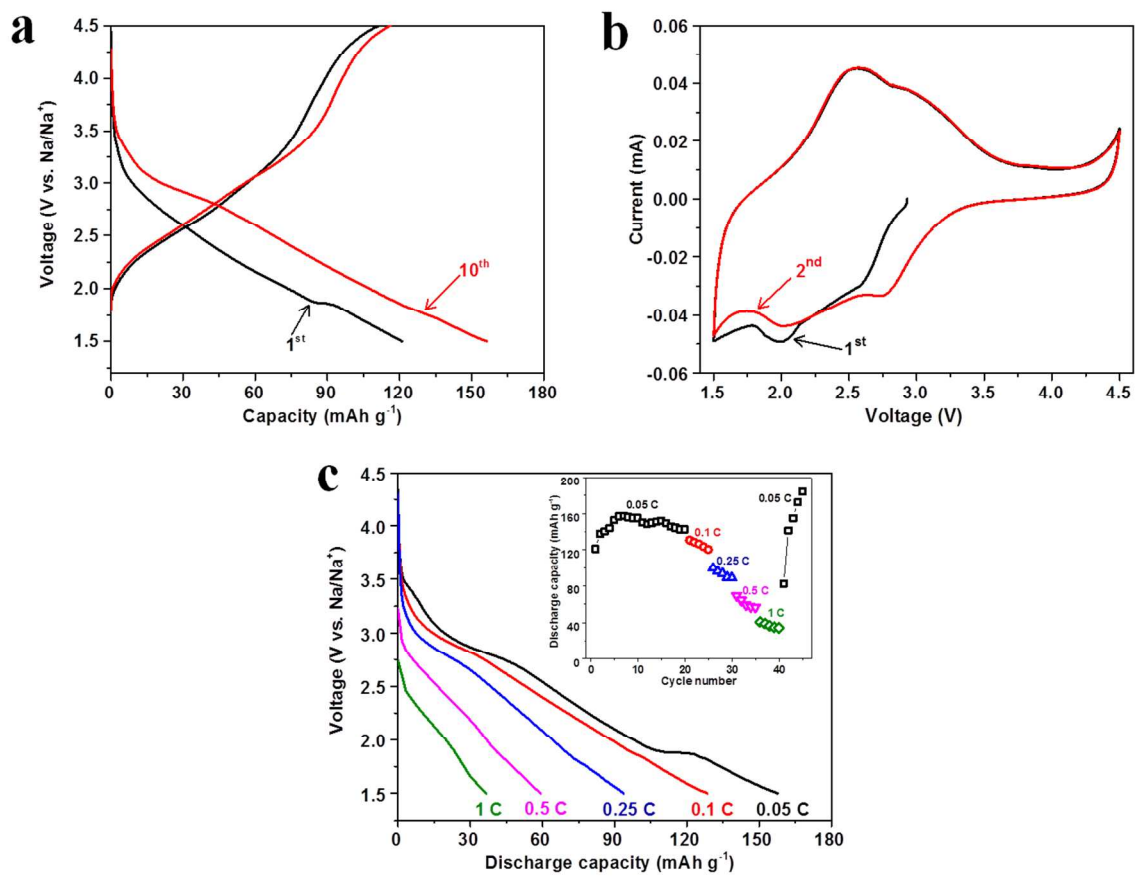


Figure 4

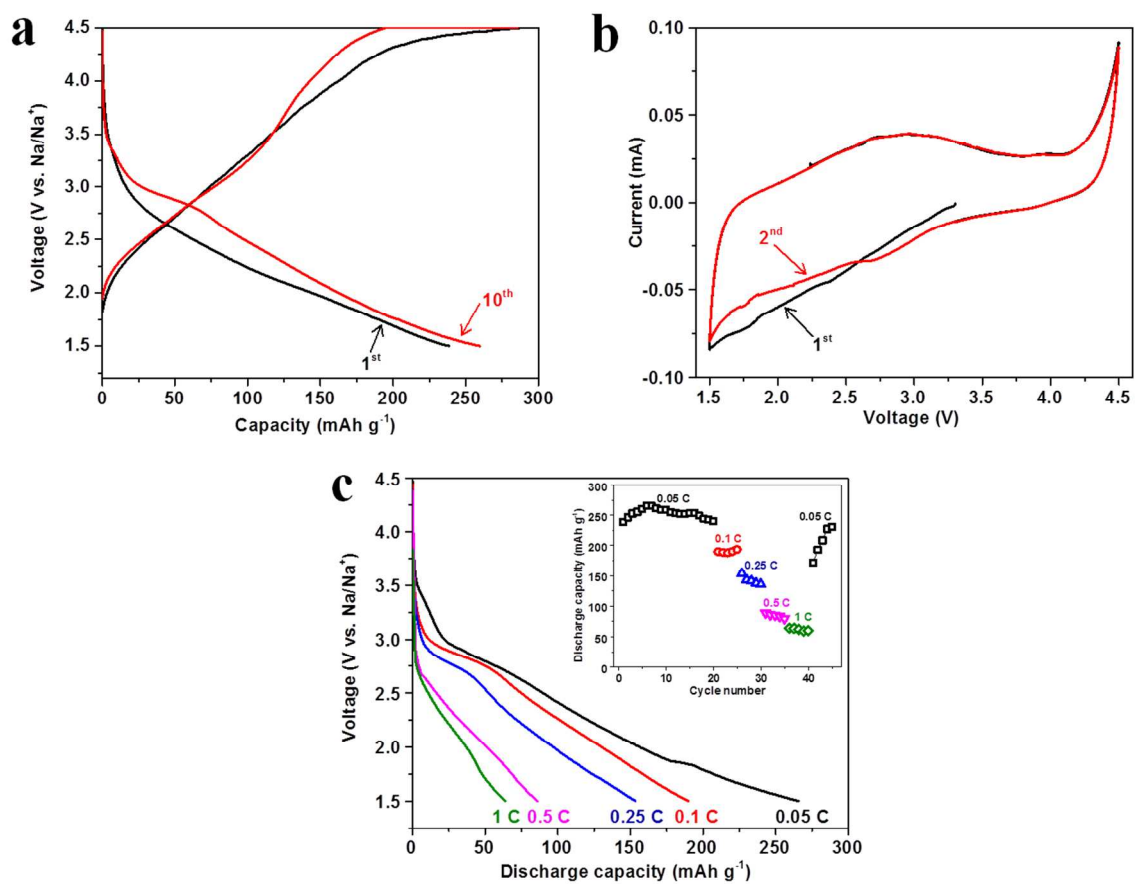


Figure 5

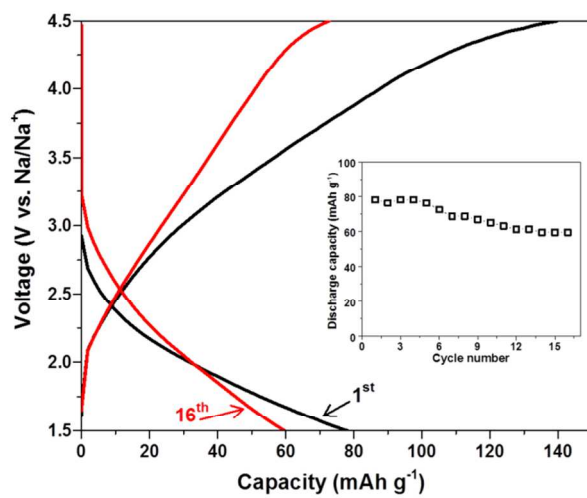


Figure 6

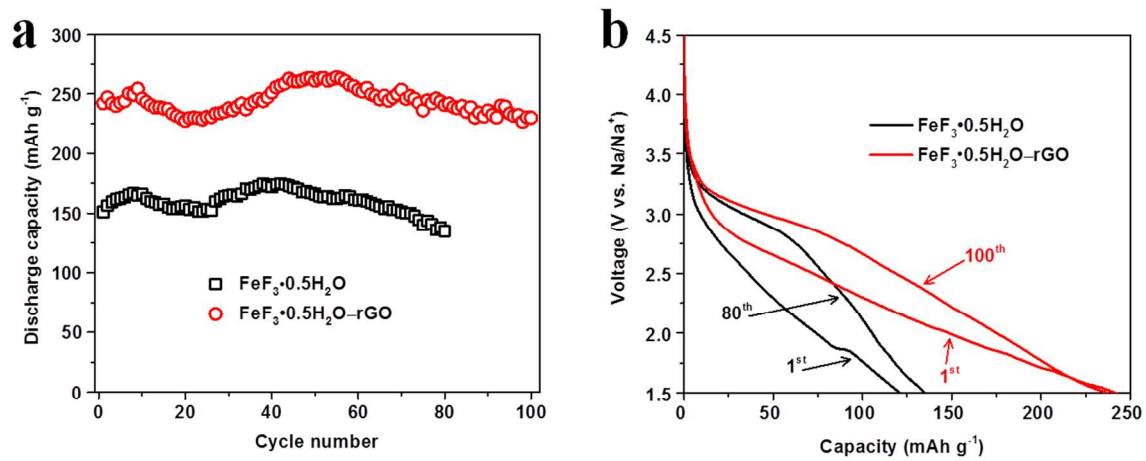


Figure 7

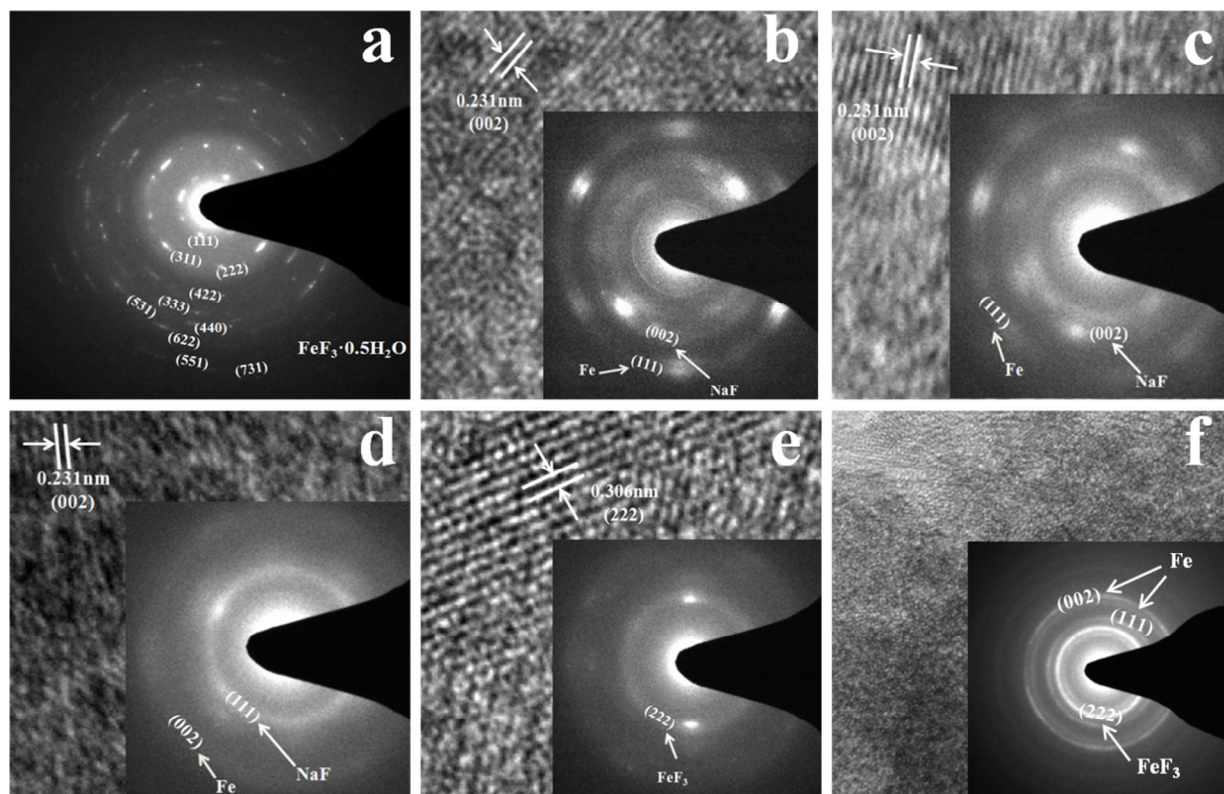


Figure 8

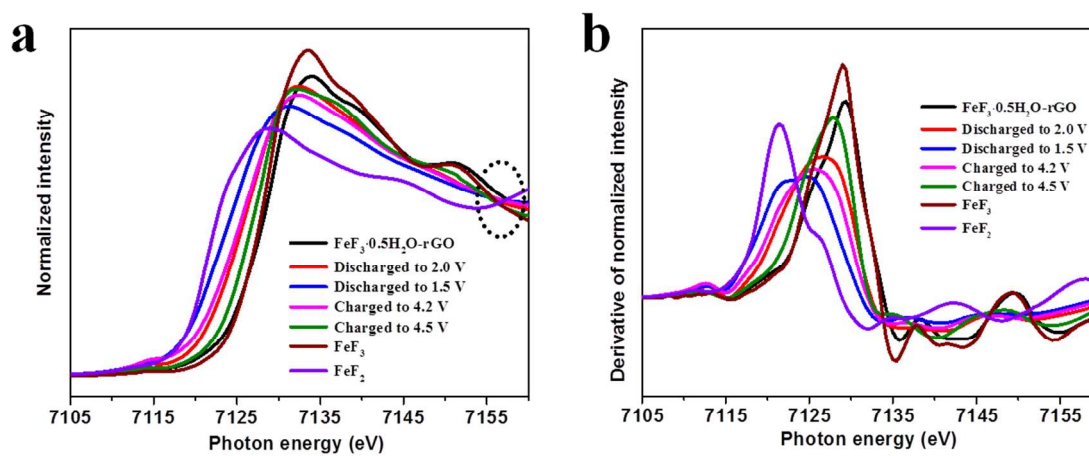


Figure 9

## References

1. P. Barpanda, G. D. Liu, C. D. Ling, M. Tamaru, M. Avdeev, S. C. Chung, Y. Yamada and A. Yamada, *Chem Mater*, 2013, 25, 3480-3487.
2. X. F. Wang, M. Tamaru, M. Okubo and A. Yamada, *J Phys Chem C*, 2013, 117, 15545-15551.
3. Y. M. Lin, P. R. Abel, A. Gupta, J. B. Goodenough, A. Heller and C. B. Mullins, *Acs Appl Mater Inter*, 2013, 5, 8273-8277.
4. H. Kim, R. A. Shakoor, C. Park, S. Y. Lim, J. S. Kim, Y. N. Jo, W. Cho, K. Miyasaka, R. Kahraman, Y. Jung and J. W. Choi, *Adv Funct Mater*, 2013, 23, 1147-1155.
5. J. F. Qian, M. Zhou, Y. L. Cao, X. P. Ai and H. X. Yang, *Adv Energy Mater*, 2012, 2, 410-414.
6. Y. H. Liu, Y. H. Xu, Y. J. Zhu, J. N. Culver, C. A. Lundgren, K. Xu and C. S. Wang, *Acs Nano*, 2013, 7, 3627-3634.
7. K. Saravanan, C. W. Mason, A. Rudola, K. H. Wong and P. Balaya, *Adv Energy Mater*, 2013, 3, 444-450.
8. H. Xiong, M. D. Slater, M. Balasubramanian, C. S. Johnson and T. Rajh, *J Phys Chem Lett*, 2011, 2, 2560-2565.
9. M. D. Slater, D. Kim, E. Lee and C. S. Johnson, *Adv Funct Mater*, 2013, 23, 947-958.
10. H. L. Pan, Y. S. Hu and L. Q. Chen, *Energ Environ Sci*, 2013, 6, 2338-2360.
11. F. Wang, R. Robert, N. A. Chernova, N. Pereira, F. Omenya, F. Badway, X. Hua, M. Ruotolo, R. G. Zhang, L. J. Wu, V. Volkov, D. Su, B. Key, M. S. Whittingham, C. P. Grey, G. G. Amatucci, Y. M. Zhu and J. Graetz, *J Am Chem Soc*, 2011, 133, 18828-18836.
12. M. Sina, K. W. Nam, D. Su, N. Pereira, X. Q. Yang, G. G. Amatucci and F. Cosandey, *J Mater Chem A*, 2013, 1, 11629-11640.
13. D.-I. Ma, Z.-y. Cao, H.-g. Wang, X.-I. Huang, L.-m. Wang and X.-b. Zhang, *Energ Environ Sci*, 2012, 5, 8538-8542.
14. Y. Yamada, T. Doi, I. Tanaka, S. Okada and J. Yamaki, *J Power Sources*, 2011, 196, 4837-4841.
15. N. Yabuuchi, M. Sugano, Y. Yamakawa, I. Nakai, K. Sakamoto, H. Muramatsu and S. Komaba, *J Mater Chem*, 2011, 21, 10035-10041.
16. T. Li, L. Li, Y. L. Cao, X. P. Ai and H. X. Yang, *J Phys Chem C*, 2010, 114, 3190-3195.
17. C. L. Li, L. Gu, J. W. Tong and J. Maier, *Acs Nano*, 2011, 5, 2930-2938.
18. L. Liu, M. Zhou, X. Y. Wang, Z. H. Yang, F. H. Tian and X. Y. Wang, *J Mater Sci*, 2012, 47, 1819-1824.
19. R. G. Ma, Z. G. Lu, C. D. Wang, H. E. Wang, S. L. Yang, L. J. Xi and J. C. Y. Chung, *Nanoscale*, 2013, 5, 6338-6343.
20. D. P. Lv, M. L. Gordin, R. Yi, T. Xu, J. X. Song, Y. B. Jiang, D. Choi and D. H. Wang, *Adv Funct Mater*, 2014, 24, 1059-1066.
21. Q. Chu, Z. Xing, J. Tian, X. Ren, A. M. Asiri, A. O. Al-Youbi, K. A. Alamry and X. Sun, *J Power Sources*, 2013, 236, 188-191.
22. Q. Chu, Z. Xing, X. Ren, A. M. Asiri, A. O. Al-Youbi, K. A. Alamry and X. Sun, *Electrochim Acta*, 2013, 111, 80-85.
23. F. Badway, F. Cosandey, N. Pereira and G. G. Amatucci, *J Electrochem Soc*, 2003, 150, A1318-A1327.
24. F. Badway, N. Pereira, F. Cosandey and G. G. Amatucci, *J Electrochem Soc*, 2003, 150, A1209-A1218.
25. I. D. Gocheva, M. Nishijima, T. Doi, S. Okada, J. Yamaki and T. Nishida, *J Power Sources*, 2009, 187, 247-252.
26. M. Nishijima, I. D. Gocheva, S. Okada, T. Doi, J. Yamaki and T. Nishida, *J Power Sources*, 2009, 190, 558-562.

27. C. L. Li, C. L. Yin, L. Gu, R. E. Dinnebier, X. K. Mu, P. A. van Aken and J. Maier, *J Am Chem Soc*, 2013, 135, 11425-11428.
28. C. L. Li, L. Gu, S. Tsukimoto, P. A. van Aken and J. Maier, *Adv Mater*, 2010, 22, 3650-+.
29. R. Depape and G. Ferey, *Mater Res Bull*, 1986, 21, 971-978.
30. S. P. Ong, V. L. Chevrier, G. Hautier, A. Jain, C. Moore, S. Kim, X. H. Ma and G. Ceder, *Energ Environ Sci*, 2011, 4, 3680-3688.
31. Y. Oumellal, A. Rougier, G. A. Nazri, J. M. Tarascon and L. Aymard, *Nat Mater*, 2008, 7, 916-921.
32. Y. S. Hong, K. S. Ryu, Y. J. Park, M. G. Kim, J. M. Lee and S. H. Chang, *J Mater Chem*, 2002, 12, 1870-1874.
33. C. L. Li, C. L. Yin, X. K. Mu and J. Maier, *Chem Mater*, 2013, 25, 962-969.
34. S. H. Park, S. M. Bak, K. H. Kim, J. P. Jegal, S. I. Lee, J. Lee and K. B. Kim, *J Mater Chem*, 2011, 21, 680-686.